One-Way and Fully-Coupled FE^2 Methods for Heterogeneous Elasticity and Plasticity Problems: Parallel Scalability and an Application to Thermo-Elastoplasticity of Dual-Phase Steels

Daniel Balzani, Ashutosh Gandhi, Axel Klawonn, Martin Lanser, Oliver Rheinbach, and Jörg Schröder

Abstract In this paper, aspects of the two-scale simulation of dual-phase steels are considered. First, we present two-scale simulations applying a top-down one-way coupling to a full thermo-elastoplastic model in order to study the emerging temperature field. We find that, for our purposes, the consideration of thermo-mechanics at the microscale is not necessary. Second, we present highly parallel fully-coupled two-scale FE^2 simulations, now neglecting temperature, using up to 458,752 cores of the JUQUEEN supercomputer at Forschungszentrum Jülich. The strong and weak parallel scalability results obtained for heterogeneous nonlinear hyperelasticity exemplify the massively parallel potential of the FE^2 multiscale method.

D. Balzani (✉) • A. Gandhi (✉)
Faculty of Civil Engineering, Institute of Mechanics and Shell Structures, TU Dresden, Dresden, Germany
e-mail: daniel.balzani@tu-dresden.de; ashutosh.gandhi@tu-dresden.de

A. Klawonn (✉) • M. Lanser (✉)
Mathematisches Institut, Universität zu Köln, Köln, Germany
e-mail: axel.klawonn@uni-koeln.de; martin.lanser@uni-koeln.de

O. Rheinbach (✉)
Institut für Numerische Mathematik und Optimierung, Technische Universität Bergakademie Freiberg, Freiberg, Germany
e-mail: oliver.rheinbach@math.tu-freiberg.de

J. Schröder (✉)
Faculty of Engineering, Department of Civil Engineering, Institute of Mechanics, Universität Duisburg-Essen, Essen, Germany
e-mail: j.schroeder@uni-due.de

H.-J. Bungartz et al. (eds.), *Software for Exascale Computing – SPPEXA 2013-2015*, Lecture Notes in Computational Science and Engineering 113,
DOI 10.1007/978-3-319-40528-5_5

1 Introduction

Advanced High Strength Steels (AHSS) provide a good combination of both, strength and formability and are therefore applied extensively in the automotive industry, especially in the crash relevant parts of the vehicle. One such AHSS which is widely employed is dual-phase (DP) steel. The excellent macroscopic behavior of this steel is a result of the inherent micro-heterogeneity and complex interactions between the ferritic and martensitic phases in the microstructure. The microstructural phases are affected by both, mechanical and thermal loads. The modeling of such steels poses a challenge because capturing all the mentioned effects leads to rather complex phenomenological models, which may still be valid for a limited number of loading scenarios.

A more promising modeling approach is the application of multiscale methods. The current contribution proposes a two-scale strategy to analyze the forming process of a DP steel sheet. In this context, the predictions of the overall mechanical response of phenomenological and multiscale-based approaches are compared. We also study the impact of considering pure mechanics versus thermo-mechanics at the microstructure on the quality of the results with view to a predictive mechanical response and the computational effort. Our scale-coupling approach for the two-scale computation of maximal stresses in largely deformed dual-phase steel sheets can be seen as a two-scale FE^2 approach with one-way coupling which consists of two steps. First, a single-scale macroscopic simulation of the deformed steel sheet based on a phenomenological material model representing the macroscopic material behavior is performed. Then, the macroscopic deformation gradient is stored at all Gauß points for each iterated load step. On the basis of macroscopic distributions of plastic strains or stresses, critical regions are identified. Second, microscopic boundary value problems are solved for all Gauß points within the critical regions. Here, the macroscopic deformation gradients are used to define the microscopic deformation-driven boundary conditions. In order to enable a higher efficiency of the scheme we propose to only compute the thermo-mechanical problem at the macroscale. Based on the temperature at each macroscopic Gauß point, we focus on a purely mechanical microscopic boundary value problem, where the temperature-dependent material parameters are updated in each load step according to the macroscopic temperature.

Compared to the high computational cost of the fully-coupled thermo-mechanical FE^2 scheme considering the temperature field at the macro- and microscale, the proposed method is clearly computationally cheaper. Furthermore, an estimator for the quality of the phenomenological macroscopic material model in the critical macroscopic region is obtained by comparing it to the homogenized material response from the microscopic computations. For the simulations including the temperature field we have made use of computing resources in Essen as well as of the CHEOPS cluster in Cologne.

The parallel scalability results for nonlinear hyperelasticity problems presented in this paper were obtained on the JUQUEEN supercomputer [30] at Forschungszentrum Jülich and make use of the FE2TI software package. The FE2TI package is a parallel implementation of the fully coupled FE^2 approach using FETI-DP (Finite Element Tearing and Interconnecting—Dual Primal) methods to solve the problems on the microscopic scale. The FE2TI package has qualified for the High-Q-Club[1] membership in 2015, and its parallel performance has previously been reported in [19, 20]. JUQUEEN is a 28,672 node 6-petaflops Blue Gene/Q system at Jülich Supercomputing Center (JSC, Germany), with a total number of 458,752 processor cores and a power consumption of 2.3 MW. It runs Linux and is ranked 11th on the TOP500 list of the world's fastest supercomputers of November 2015. It uses a Power BQC 16C 1.6 GHz processor with 16 cores and 16 GB memory per node.

The paper is organized in various sections. The material model and a numerical differentiation scheme based on complex step derivative approximation (CSDA) that has been used in the implementation of numerical examples of the one-way coupling FE^2 method are briefly discussed in Sect. 2. A short summary of the general FE^2 multiscale method and the one-way scale-coupling strategy introduced here to study the DP steel sheet response is given in Sect. 3. The details regarding the numerical example and the results obtained with the various strategies are then illustrated in Sect. 4. In Sect. 5 the parallel implementation of the FE^2 method is described, weak parallel scalability for production runs up to the complete JUQUEEN are presented, and strong parallel scalability results for up to 131,072 cores are reported. Finally, the conclusion is presented in Sect. 6.

2 Thermodynamic and Continuum Mechanical Framework

We now present the thermo-elastoplastic framework used in our one-way scale-coupling method. Thermo-mechanics at finite strains are governed by the balance equation of linear momentum and energy. In this section, we only recapitulate the main results of the formulation in the reference configuration, given as

$$-\operatorname{Div}\mathbf{F}\,\mathbf{S}-\mathbf{f}=\mathbf{0}\,, \tag{1}$$

$$\mathbf{S}\cdot\frac{1}{2}\dot{\mathbf{C}}+\rho_0 r-\operatorname{Div}\mathbf{q}_0-\rho_0(\dot{\Psi}+\dot{\overline{\theta\eta}})=0\,, \tag{2}$$

and refer the interested reader to [15] for a detailed derivation of these equations and the corresponding weak forms required for the finite element implementation. In equation (2), the Legendre transformation $\Psi = U - \theta\eta$ has been performed, where Ψ, U, η and θ denote the Helmholtz free energy, the specific internal energy, the specific entropy and the temperature, respectively, cf. [33] and [28]. $\mathbf{S}$ denotes

[1] http://www.fz-juelich.de/ias/jsc/EN/Expertise/High-Q-Club/FE2TI/_node.html

the second Piola-Kirchoff stress tensor, $\mathbf{C} = \mathbf{F}^T\mathbf{F}$ represents the right Cauchy Green deformation tensor, $\mathbf{F} = \text{Grad}\boldsymbol{\varphi}$ is the deformation gradient and $\boldsymbol{\varphi}$ defines the nonlinear deformation map, which maps points $\mathbf{X}$ of the undeformed reference configuration $\mathscr{B}_0$ onto points $\mathbf{x}$ of the deformed (actual) configuration. Note that a simple dot notation is used in $\mathbf{S} \cdot \dot{\mathbf{C}}$ to express the full contraction of $\mathbf{S}$ and $\dot{\mathbf{C}}$. $\mathbf{q}_0$ is the heat flux through the body in the reference configuration, which is related to the Cauchy heat flux $\mathbf{q} = -k_\theta \text{grad}\theta$ by $\mathbf{q_0} = J\mathbf{F}^{-1}\mathbf{q}$. Herein, k_θ is the isotropic heat conduction coefficient and J is the determinant of $\mathbf{F}$. The operators Grad(•) and grad(•) denote the gradient with respect to coordinates in the reference and actual configuration. Also, $\mathbf{f}$, r and ρ_0 are the body force vector, internal heat source and the reference density of the body, respectively. Applying the standard Galerkin method, the weak forms of these balance equations can be derived, see e.g. [34] or [28]. Herein, approximations for the displacements in the sense of isoparametric finite elements are inserted. Thus the system to be solved can be written as

$$G_{\mathrm{u}} = G_{\mathrm{u}}^{\mathrm{int}} - G_{\mathrm{u}}^{\mathrm{ext}} \approx \sum_{e=1}^{n_{\mathrm{ele}}} (\delta \mathbf{d}_{\mathrm{u}}^{e})^{\mathrm{T}} \left[\mathbf{r}_{\mathrm{u}}^{e,\mathrm{int}} - \mathbf{r}_{\mathrm{u}}^{e,\mathrm{ext}} \right] = 0 \,, \tag{3}$$

$$G_{\theta} = G_{\theta}^{\mathrm{int}} - G_{\theta}^{\mathrm{ext}} \approx \sum_{e=1}^{n_{\mathrm{ele}}} (\delta \mathbf{d}_{\theta}^{e})^{\mathrm{T}} \left[\mathbf{r}_{\theta}^{e,\mathrm{int}} - \mathbf{r}_{\theta}^{e,\mathrm{ext}} \right] = 0 \,, \tag{4}$$

where 'G' denotes the weak forms, while the elemental residuals and degree of freedom vectors are introduced as $\mathbf{r}^e$ and $\mathbf{d}^e$ respectively. Here, the subscripts 'u' and 'θ' represent the mechanical and thermal contributions, respectively, and n_{ele} is the number of elements.

2.1 Incorporation of Thermo-mechanics

Since advanced high strength steels are fundamentally thermo-mechanical in nature, the study presented here employs a thermo-elastoplastic material model, as established in [33] and [28]. The main features of the implementation are briefly described in this section. The deformation gradient is multiplicatively decomposed into an elastic ($\mathbf{F}^e$) and a plastic part ($\mathbf{F}^p$) such that $\mathbf{F} = \mathbf{F}^e\mathbf{F}^p$. The isotropic free energy function, incorporating isotropic hardening, takes the form $\Psi = \Psi(\mathbf{b}^e, \theta, \alpha)$, where $\mathbf{b}^e = \mathbf{F}^e\mathbf{F}^{e\mathrm{T}}$ and α represent the left Cauchy-Green deformation tensor and the equivalent plastic strain, respectively. The internal dissipation consists of a mechanical and a thermal contribution, $\mathscr{D}_{\mathrm{int}} = \mathscr{D}_{\mathrm{mech}} + \mathscr{D}_{\mathrm{therm}}$. The expressions for these are obtained using the principle of maximum dissipation, the evolution equations for the internal variables $\mathbf{b}^e$, α and the Kuhn-Tucker optimality conditions. For a von Mises type limit surface, the mechanical part reduces to $\mathscr{D}_{\mathrm{mech}} = \lambda\sqrt{\frac{2}{3}}y(\theta)$, where λ is the consistency parameter and $y(\theta)$ the temperature dependent initial yield stress. Exploiting the entropy inequality and Gauß-theorem in (1)

and (2) leads upon discretization to the detailed form of the elemental residual vectors

$$\mathbf{r}_{\mathrm{u}}^{e,\mathrm{int}} = \sum_{I=1}^{nen} \int_{\mathscr{B}_0^e} (\mathbf{B}_{\mathrm{u}}^I)^{\mathrm{T}} \mathbf{S} \, \mathrm{d}V \,, \tag{5}$$

$$\begin{aligned} \mathbf{r}_{\theta}^{e,\mathrm{int}} = \sum_{I=1}^{nen} \int_{\mathscr{B}_0^e} \Big((\mathbf{B}_{\theta}^I)^{\mathrm{T}} \mathbf{q}_0 \; & + N^I \rho_0 \theta \partial^2_{\theta\theta} \Psi \dot{\theta} + N^I \rho_0 \theta \partial^2_{\theta\alpha} \Psi \, \dot{\alpha} \\ & + N^I \rho_0 \theta \partial^2_{\theta \mathbf{b}^{\mathrm{e}}} \Psi \cdot \dot{\mathbf{b}}^{\mathrm{e}} + N^I \lambda \sqrt{\tfrac{2}{3}} y(\theta) \Big) \, \mathrm{d}V \,. \end{aligned} \tag{6}$$

Here, $\mathbf{B}_{\mathrm{u}}$ and $\mathbf{B}_{\theta}$ matrices hold the derivatives of the shape functions with respect to spatial coordinates, cf. [4], the $(\dot{\bullet})$ represents the material time derivative of $(\bullet)$ and *nen* is the number of nodes per element. Note that in the current work we use an additively decoupled, isotropic free energy function with a mechanical part $\Psi^{\mathrm{e}}_{\mathrm{vol}} + \Psi^{\mathrm{e}}_{\mathrm{iso}} + \Psi^{\mathrm{p}}$, a thermo-mechanical coupling part Ψ^{c} and thermal part Ψ^{θ}, i.e. $\Psi = \Psi^{\mathrm{e}}(\mathbf{b}^{\mathrm{e}}) + \Psi^{\mathrm{p}}(\alpha) + \Psi^{\mathrm{c}}(\mathbf{b}^{\mathrm{e}}, \theta) + \Psi^{\theta}(\theta)$, with the individual parts

$$\begin{aligned} \Psi^{\mathrm{e}}_{\mathrm{vol}} &= \tfrac{\kappa}{\rho_0} \left[\tfrac{1}{2}(J^2 - 1) - \ln J \right] \,, \\ \Psi^{\mathrm{e}}_{\mathrm{iso}} &= \tfrac{\mu}{2\rho_0} \left[\mathrm{tr}\mathbf{b}^{\mathrm{e}} (\det \mathbf{b}^{\mathrm{e}})^{-1/3} - 3 \right] \,, \\ \Psi^{\mathrm{p}} &= \tfrac{1}{2\rho_0} H \, \alpha^2 \,, \\ \Psi^{\mathrm{c}} &= -\tfrac{3}{\rho_0} \alpha_{\mathrm{t}} \, (\theta - \theta_0) \, \partial_J \Psi^{\mathrm{e}}_{\mathrm{vol}} \,, \\ \Psi^{\theta} &= -\rho_0 \, c \left(\theta \ln \tfrac{\theta}{\theta_0} - \theta + \theta_0 \right) \,. \end{aligned} \tag{7}$$

For the yield stress $y(\theta)$, a linearly decreasing function in terms of the temperature is considered. Here, H is the linear isotropic hardening modulus for plasticity. The external residual vectors in Eqs. (3) and (4) are obtained on discretizing the external parts of the weak form consisting of the traction vectors and the surface heat fluxes for mechanical and thermal contributions respectively, cf. [34]. These are not discussed here for conciseness of the text; for further details on the algorithmic treatment of thermoplasticity see [28].

2.2 *Implementation Using a Complex Step Derivative Approximation*

Two widely used numerical differentiation schemes, namely the finite difference method (FD) and the Complex Step Derivative Approximation (CSDA) approach, have been employed to evaluate the stiffness matrix in nonlinear finite element simulations; cf. [22, 25]. Another successful approach is Automatic Differentiation (AD) and, interestingly, relations of CSDA to the forward mode of AD have been pointed out [13]. All these approaches eliminate the need to compute analytical

linearizations of the weak forms, which is especially useful in the early development stage of elaborate material models. However, the FD approach leads to round-off errors for small step sizes. The CSDA based strategy overcomes this issue by applying perturbations (of size h) along the imaginary axis of the complex number (cf. [31]) and thus permits the choice of perturbations at the order of the machine precision. Thus, although the method is a (second order) approximation, as with AD, local quadratic convergence can be expected. The implementation of CSDA is simple, especially if a Fortran FD implementation is already available, since Fortran and Fortran libraries have handled complex numbers consistently for a long time. The computational cost, however, is typically larger than for the forward mode of AD.

Our implementation of CSDA was extended also to nonlinear thermo-mechanical problems, where again quadratic convergence rates were obtained; see [4]. A brief summary of this method is presented here. Considering conservative loading and the functional dependencies of the residuals, i.e., $\mathbf{r}_{\mathrm{u}}^{e,\mathrm{int}} := \mathbf{r}_{\mathrm{u}}^{e,\mathrm{int}}(\mathbf{d}_{\mathrm{u}}^{e}, \mathbf{d}_{\theta}^{e})$ and $\mathbf{r}_{\theta}^{e,\mathrm{int}} := \mathbf{r}_{\theta}^{e,\mathrm{int}}(\mathbf{d}_{\mathrm{u}}^{e}, \mathbf{d}_{\theta}^{e})$, the linearized increments are obtained by differentiating $\mathbf{r}_{\mathrm{u}}^{e,\mathrm{int}}$ and $\mathbf{r}_{\theta}^{e,\mathrm{int}}$ with respect to both $\mathbf{d}_{\mathrm{u}}^{e}$ and $\mathbf{d}_{\theta}^{e}$ and can be written as

$$\Delta G_{\mathrm{u}}^{\mathrm{int,h}} \approx \sum_{e=1}^{n_{\mathrm{ele}}} (\delta \mathbf{d}_{\mathrm{u}}^{e})^{\mathrm{T}} \left(\mathbf{k}_{\mathrm{uu}}^{e} \, \Delta \mathbf{d}_{\mathrm{u}}^{e} + \mathbf{k}_{\mathrm{u}\theta}^{e} \, \Delta \mathbf{d}_{\theta}^{e} \right) , \tag{8}$$

$$\Delta G_{\theta}^{\mathrm{int,h}} \approx \sum_{e=1}^{n_{\mathrm{ele}}} (\delta \mathbf{d}_{\theta}^{e})^{\mathrm{T}} \left(\mathbf{k}_{\theta\mathrm{u}}^{e} \, \Delta \mathbf{d}_{\mathrm{u}}^{e} + \mathbf{k}_{\theta\theta}^{e} \, \Delta \mathbf{d}_{\theta}^{e} \right) . \tag{9}$$

Now the CSDA scheme can be used to evaluate the stiffness matrix contributions. The approximations of the k-th column vectors $\tilde{\mathbf{k}}_{\mathrm{uu}(k)}^{e}$ and $\tilde{\mathbf{k}}_{\theta\mathrm{u}(k)}^{e}$ in $\mathbf{k}_{\mathrm{uu}}^{e}$ and $\mathbf{k}_{\theta\mathrm{u}}^{e}$, respectively, and of the j-th column vectors $\tilde{\mathbf{k}}_{\mathrm{u}\theta(j)}^{e}$ and $\tilde{\mathbf{k}}_{\theta\theta(j)}^{e}$ in $\mathbf{k}_{\mathrm{u}\theta}^{e}$ and $\mathbf{k}_{\theta\theta}^{e}$, respectively, are given by

$$\begin{aligned}
\tilde{\mathbf{k}}_{\mathrm{uu}(k)}^{e} &:= \frac{\partial \mathbf{r}_{\mathrm{u}}^{e,\mathrm{int}}}{\partial \left\{ d_{\mathrm{u}}^{e} \right\}_{k}} \approx \frac{\Im \left[\mathbf{r}_{\mathrm{u}}^{e}(\mathbf{d}_{\mathrm{u}}^{e} + ih\tilde{\mathbf{d}}_{\mathrm{u}(k)}^{e}, \mathbf{d}_{\theta}^{e}) \right]}{h} , \\
\tilde{\mathbf{k}}_{\mathrm{u}\theta(j)}^{e} &:= \frac{\partial \mathbf{r}_{\mathrm{u}}^{e,\mathrm{int}}}{\partial \left\{ d_{\theta}^{e} \right\}_{j}} \approx \frac{\Im \left[\mathbf{r}_{\mathrm{u}}^{e}(\mathbf{d}_{\mathrm{u}}^{e}, \mathbf{d}_{\theta}^{e} + ih\tilde{\mathbf{d}}_{\theta(j)}^{e}) \right]}{h} , \\
\tilde{\mathbf{k}}_{\theta\mathrm{u}(k)}^{e} &:= \frac{\partial \mathbf{r}_{\theta}^{e,\mathrm{int}}}{\partial \left\{ d_{\mathrm{u}}^{e} \right\}_{k}} \approx \frac{\Im \left[\mathbf{r}_{\theta}^{e}(\mathbf{d}_{\mathrm{u}}^{e} + ih\tilde{\mathbf{d}}_{\mathrm{u}(k)}^{e}, \mathbf{d}_{\theta}^{e}) \right]}{h} , \\
\tilde{\mathbf{k}}_{\theta\theta(j)}^{e} &:= \frac{\partial \mathbf{r}_{\theta}^{e,\mathrm{int}}}{\partial \left\{ d_{\theta}^{e} \right\}_{j}} \approx \frac{\Im \left[\mathbf{r}_{\theta}^{e}(\mathbf{d}_{\mathrm{u}}^{e}, \mathbf{d}_{\theta}^{e} + ih\tilde{\mathbf{d}}_{\theta(j)}^{e}) \right]}{h} ,
\end{aligned} \tag{10}$$

where the indices $k \in [1, tdof_{\mathrm{u}}]$ and $j \in [1, tdof_{\theta}]$ on the left hand side of the equations represent the column index. On the right hand side these indices

correspond to the individual perturbation vectors $\tilde{\mathbf{d}}^e$ whose components with indices $m \in [1, tdof_{\mathrm{u}}]$ and $q \in [1, tdof_\theta]$, respectively, are defined as

$$\{\tilde{d}^e_{\mathrm{u}(k)}\}_m = \delta_{(k)m} \quad \text{and} \quad \{\tilde{d}^e_{\theta(j)}\}_q = \delta_{(j)q} \,. \tag{11}$$

Herein, the Kronecker symbol is defined as $\delta_{ab} = 1$ for $a = b$ and $\delta_{ab} = 0$ otherwise. $tdof_u$ and $tdof_\theta$ are the total mechanical and thermal elemental degrees of freedoms, respectively, and $\Im$ is the imaginary operator.

3 Framework for Direct-Micro-Macro Computations

The direct micro-macro approach for computation of material behavior of micro-heterogeneous materials has been well-developed in the last 15 years, see e.g. [9–12, 23, 24, 29], see also [27]. For sake of completeness, in the following subsection this method is briefly recapitulated. Thereafter in Sect. 3.2, we discuss the multiscale treatment proposed here to model DP steel sheet behavior.

3.1 General Approach

The general FE^2 concept involves solving a microscopic boundary value problem at each macroscopic integration point during the solution of the macroscopic boundary value problem. These nested problems are defined on representative volume elements (RVEs) that describe the complex geometry of the microstructure adequately. Appropriate boundary conditions are applied to these in terms of, e.g., the deformation gradients at the macroscopic integration point. After solving the microscopic problem, suitable volume averages of microscopic stresses $\mathbf{P}$ and microscopic tangent moduli $\mathbb{A}$ are computed and returned back to the macroscopic integration point, which replaces the evaluation of a classical phenomenological macroscopic material law.

These averages are computed as

$$\overline{\mathbf{P}} = \frac{1}{V}\int_{\mathscr{B}_0} \mathbf{P}\,\mathrm{d}V \quad \text{and} \quad \overline{\mathbb{A}} = \frac{1}{V}\int_{\mathscr{B}_0} \mathbb{A}\,\mathrm{d}V - \frac{1}{V}\mathbf{L}^{\mathrm{T}}\mathbf{K}^{-1}\mathbf{L}\,, \quad \mathbf{L} = \int_{\mathscr{B}_0} \mathbf{B}^{\mathrm{T}}\mathbb{A}\mathrm{d}V\,. \tag{12}$$

Here, $\overline{\mathbf{P}}$, $\overline{\mathbb{A}}$ represent the macroscopic first Piola-Kirchhoff stresses and the macroscopic material tangent moduli. The global stiffness matrix and the spatial derivatives of the shape functions of the microscopic boundary value problem are denoted by $\mathbf{K}$ and $\mathbf{B}$, respectively. This procedure eliminates the need of a phenomenological law at the macroscale. Furthermore, certain effects like anisotropy, and its evolution as well as kinematic hardening are automatically included through the solution of the micro-problem due to its heterogeneity.

Algorithm 1 Algorithmic description of the FE^{2}TI approach. Overlined letters denote macroscopic quantities. This algorithm consists of the classical FE^2 scheme using (ir)FETI-DP for solving the microscopic boundary value problems. We consider all macroscopic as well as microscopic Newton iterations as converged, if the l_2-norm of the Newton update is smaller than $1e-6$. The GMRES iteration in our FETI-DP methods is stopped, if a relative residual reduction of $1e-8$ is reached. This pseudocode is taken from [20]

Repeat until convergence of the Newton iteration:

1. Apply boundary conditions to RVE (representative volume element) based on macroscopic deformation gradient: Enforce $x = \overline{F}X$ on the boundary of the microscopic problem $\partial\mathscr{B}$ in the case of Dirichlet constraints.
2. Solve one microscopic nonlinear implicit boundary value problem for each macroscopic Gauß point using Newton-Krylov-(ir)FETI-DP or related methods.
3. Compute and return macroscopic stresses as volumetric average of microscopic stresses $\mathbf{P}^h$:
$$\overline{P}^h = \frac{1}{V}\sum_{T\in\tau}\int_T P^h dV\,.$$
4. Compute and return macroscopic tangent moduli as average over microscopic tangent moduli $\mathbb{A}^h$:
$$\overline{\mathbb{A}}^h = \frac{1}{V}\left(\sum_{T\in\tau}\int_T \mathbb{A}^h\, dV\right) - \frac{1}{V}L^T\,(K)^{-1}\,L\,.$$
5. Assemble tangent matrix and right hand side of the linearized macroscopic boundary value problem using $\overline{P}^h$ and $\overline{\mathbb{A}}^h$.
6. Solve linearized macroscopic boundary value problem.
7. Update macroscopic deformation gradient $\overline{F}$.

Note that, because of the two-scale procedure, the Newton linearization of the FE^2 method was not straight forward but rather a significant step in the development of the method. In our fully coupled FE^2 simulations, we use a consistent Newton linearization and thus can expect locally quadratic convergence of the fully coupled two-scale method, i.e., of the outermost loop in Algorithm 1.

For a brief description of the algorithm and an efficient parallel implementation, see also Sect. 5.1 and Algorithm 1.

3.2 Approaches for Multiphase-Steel Incorporating Thermo-mechanics

Two-scale analysis is performed to study the influence of macroscopic deformation on the microscopic mechanical fields to obtain more realistic simulations of sheet

metal forming processes. For efficiency reasons, here, we focus on a one-way scale-coupling scheme, using efficient parallel algorithms to solve complex microscopic boundary value problems of DP steel microstructures. For that purpose we first perform a thermo-mechanical simulation of the macroscopic sheet metal forming process using a phenomenological thermo-elastoplastic material model at finite strains, as described in Sect. 2, which would be used in engineering practice. Then, in order to obtain more information of those mechanical fields at the microscale which are important for failure initialization analysis, the macroscopic regime with high plastic strains is identified. Only there, additional microscopic boundary value problems are solved which are driven by the macroscopic deformation gradients and temperatures computed at the macroscopic integration points. In detail, regarding the displacements, linear displacement boundary conditions are applied to the real DP steel microstructures and periodic boundary conditions are considered when using statistically similar RVEs (Representative Volume Elements) in the sense of [5]. The microstructure consists of two phases—ferrite as the matrix phase and martensite as the inclusion phase.

With respect to the temperature, we focus on different approaches: (i) the temperature calculated at the macroscopic integration point is applied to the boundary of the microscopic boundary value problem, where thermo-mechanics are considered and the temperature is free to evolve, and (ii) the microscopic thermal fluctuations are considered to be small due to small deviations of thermo-mechanical parameters for ferrite and martensite. Therefore, only mechanical boundary value problems taking into account temperature-dependent yield stresses are considered at the microscale. The latter approach enables more efficient computations since the temperature is not a degree of freedom in the microscopic calculations anymore. Simulations based on such one-way scale-couplings have two important advantages compared with purely macroscopic computations: first, they provide valuable information regarding those microscopic mechanical fields in the macroscopic domains where failure is expected to initialize. Second, an estimation of the quality of the macroscopic material model is obtained by comparing to the more accurate micro-macro computation.

4 Numerical Examples for the One-Way FE^2 Coupling

In the analysis performed here, we consider at the macroscale the extension of a DP steel sheet containing a regular arrangement of holes. The dimensions of the sheet and the diameter of the holes are $140 \times 140 \times 6$ mm and 20 mm, respectively. A displacement of 10 mm is applied in X-direction at the outer surface of the sheet such that the metal sheet is extended up to 14.28 % nominal strain. The time considered for this deformation is 10 s. Due to the symmetry of the problem, we only simulate 1/8th of the plate, see Fig. 1a, and incorporate appropriate symmetry conditions. The plate is discretized with 10-noded tetrahedral finite elements. As a phenomenological description at the macroscale, we consider the thermo-

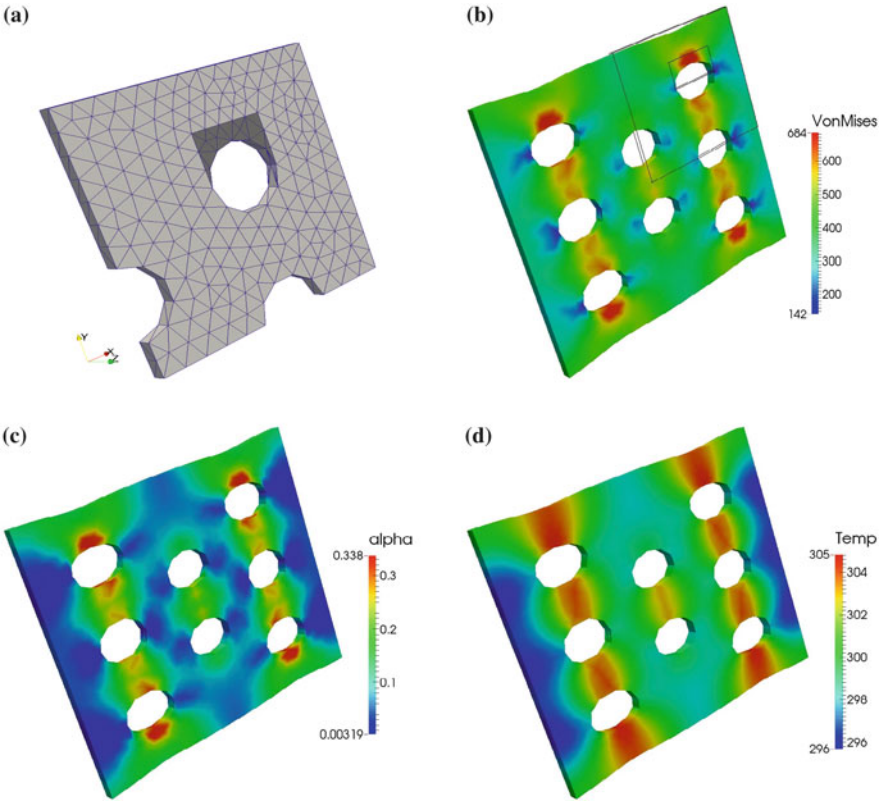

Fig. 1 **(a)** 1/8th geometry of the plate with tetrahedral finite element mesh, macroscopic **(b)** von Mises stress, **(c)** equivalent plastic strain and **(d)** temperature distributions in the deformed configuration of the sheet metal after applying full extension at the macro-level

mechanical formulation of [28], which was implemented using the new CSDA scheme. The initial yield stress as well as the linear hardening modulus were adjusted to yield curves calculated as volumetric averages of purely mechanical micro-macro computations of uni-axial tension tests. The hardening modulus was chosen such that the model response matches this yield curve at approximately 30 % strain. In the micro-macro computations the same thermo-mechanical framework was used as in the macroscopic computations. The resulting distributions of stress, equivalent plastic strains and temperature are as shown in Fig. 1b–d, respectively. As can be seen, the fluctuation of temperature is rather small although rather large plastic strains are obtained. However, in particular for the detection of necking, the incorporation of even small temperature deviations may be essential, cf. the findings in [28]. In Fig. 1a the eighth of the complete sheet metal considered for computation is depicted. Additionally, the outline of a subregion is marked which is considered as most critical for failure initialization since here the largest macroscopic stresses

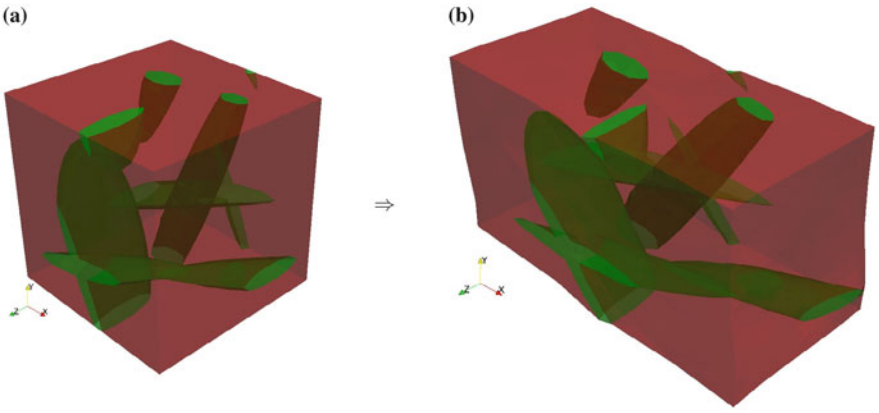

Fig. 2 **(a)** Undeformed SSRVE structure for evaluation of the microscopic problem at the point of interest indicated by the bullet and **(b)** deformed configuration of the SSRVE at full load

are found. This subregion is therefore considered as the most relevant regime, and detailed micro-macro computations are performed, here. For this purpose, there the deformation gradient and the temperature at each macroscopic integration point is stored for every load step in order to be applied in subsequent microscopic computations.

In order to analyze the influence of the two approaches (i) and (ii) we focus on statistically similar RVEs (SSRVEs) which were computed for DP steel in [5]; cf. Fig. 2a. For the analysis, we consider a macroscopic integration point within the critical region, where its position is marked by the bullet in Fig. 1a. The hardening modulus for the pure ferrite and the pure martensite is chosen such that the model response corresponds to the experimental yield stress in uni-axial tension at 10 % strains. The distributions of von Mises stresses and equivalent plastic strains as a result of the thermo-mechanical computations associated with approach (i) are depicted in Fig. 3. They indicate a higher development of stresses and negligible plastic strains in the martensitic inclusions. The ferritic matrix phase shows lower stresses and higher plastic strains are accumulated here due to the lower yield stress as compared to the martensite.

For the purely mechanical microscopic computation the temperature-dependent initial yield stress y is taken into account such that $y = \langle \omega(\theta - \theta_0) + y_0 - \tilde{y}_0 \rangle + \tilde{y}_0$, where the Macauley brackets $\langle(\bullet)\rangle = \frac{1}{2}[|(\bullet)| + (\bullet)]$ ensure a limiting yield stress $\tilde{y}_0$. Herein, θ, θ_0 and ω are the current temperature, the room temperature and a thermal softening parameter; y_0 denotes the initial yield stress at room temperature. When comparing the stresses and plastic strains resulting from the purely mechanical computation where the temperature-dependent yield behavior is incorporated (approach (ii)), see Fig. 4, we obtain quite similar distributions at the microscale. This is also observed for the macroscopic values: the macroscopic von

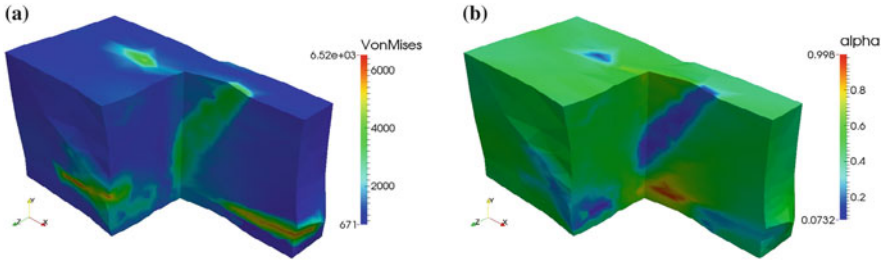

Fig. 3 **(a)** Von Mises stresses and **(b)** equivalent plastic strain distributions at full macroscopic deformation for the thermo-mechanical microstructure computations according to approach (i). The SSRVE, see Fig. 2b, has been clipped to visualize the interior

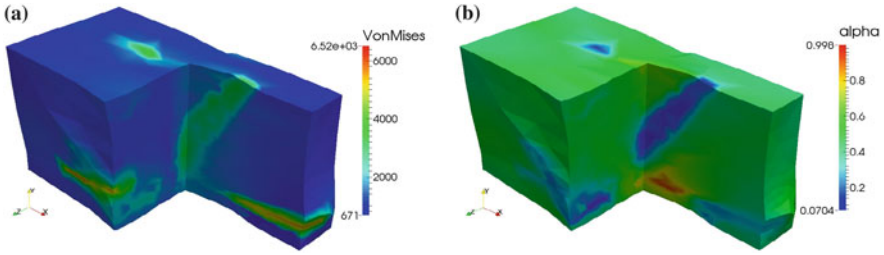

Fig. 4 **(a)** Von Mises stresses and **(b)** equivalent plastic strain distributions over the SSRVE at full macroscopic deformation for the purely mechanical calculations according to approach (ii). The SSRVE, see Fig. 2b, has been clipped to visualize the interior

Mises stress is computed from the volume averaged Cauchy stress and takes a value of 1050.4 MPa, whereas for the thermo-mechanical computation it is 1009.85 MPa.

Now, we compare the results of the micro-macro computations with the response of the purely macroscopic phenomenological model. Therefore, the macroscopic von Mises stress versus nominal extension at the bullet point in the sheet metal is plotted in Fig. 5a. As can be seen, the difference between the purely macroscopic computation and the micro-macro computation is rather large, compared to the difference between the two approaches (i) and (ii). Furthermore, Fig. 5b shows the temperature distribution at the microscale as a result of approach (i). A quite small fluctuation even below 1 K is observed. This indicates that the consideration of thermo-mechanics at the microscale is not necessarily required. In Fig. 5a also the response of a purely mechanical micro-macro computation is plotted, where not even the temperature dependency of the yield stress is taken into account. A small deviation from the computation including temperature-dependent yield stresses is observed. However, the incorporation of temperature-dependent evolving yield stresses may be important in order to accurately represent a potential necking at the microscale, cf. [28]. Therefore, in the following, the model based on approach (ii) is used to perform parallel micro-macro simulations of the entire critical region as seen in Fig. 1a which consists of 468 microscopic boundary value problems associated with the macroscopic integration points. We consider realistic microstructures with

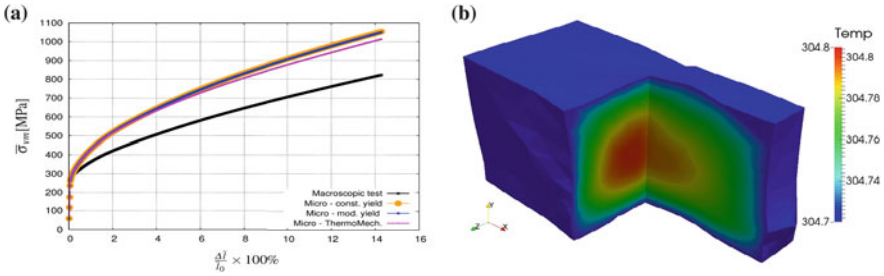

Fig. 5 **(a)** Comparison of the macroscopic von Mises stress vs. nominal strain curves resulting from the macroscopic phenomenological law and from the micro-macro computations and **(b)** bi-sectional view of the temperature distribution at the microscale as a result of approach (i)

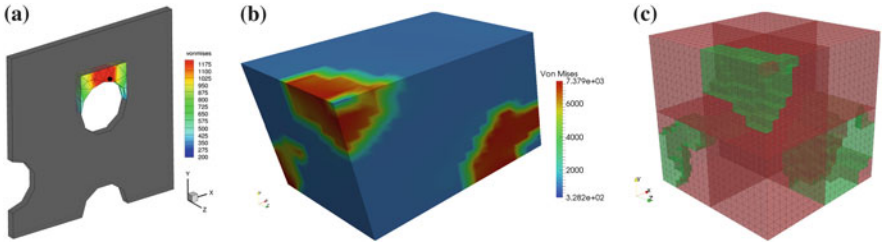

Fig. 6 **(a)** Von Mises stresses in the critical region after applying the full extension obtained from averaging the stress distributions from the microscopic boundary value problems with the **(c)** realistic microstructure; **(b)** von Mises stresses in the deformed configuration of one exemplary microscopic boundary value problem corresponding to the macroscopic integration point *P* marked with the *black dot* in Fig. 6a

206,763 degrees of freedom each, see Fig. 6c. For an efficient and fast solution we decomposed the microstructure in eight cubical subdomains and used a Newton-Krylov FETI-DP approach. All microscopic computations have been performed on eight cores of the CHEOPS cluster at the RRZK in Cologne. In Fig. 6b we present the von Mises stresses in the deformed configuration of one exemplary microscopic problem and in Fig. 6b the von Mises stresses in the complete critical region of the macroscopic problem. The von Mises stresses in the integration points of the macroscopic problem are obtained from a suitable volumetric average over the microscopic quantities. When comparing the results with the purely macroscopic computations shown in Fig. 1a, the qualitative distribution of the stresses looks similar. The quantitative results differ however more than 30 %, which shows the necessity to analyze scale-coupled computations. In addition to a more reliable prediction of stresses at the macroscale, microscopic stress distributions are available building the basis for failure initialization analysis. We additionally provide a brief summary of the RVE computations performed on CHEOPS and using FETI-DP for the solution of all linear systems; see Table 1.

Table 1 RVEs using the J2 plasticity material model in 3D. For the three dimensional micro structure; see Fig. 6c. *Average Newton It.* denotes the number of Newton iterations per RVE, summed up over all macroscopic load steps and averaged over all RVEs

Realistic RVEs with thermo-plasticity and realistic microstructure				
#RVEs	D.o.f. per RVE	FETI-DP subdomains per RVE	Average Newton It.	Total core× h
468	206,763	8	2113	9.28 h × 8 × 468

5 FE2TI: A Parallel Implementation of the Fully Coupled FE^2 Approach

The FE2TI software is a parallel implementation of the (fully coupled) FE^2 method using FETI-DP domain decomposition methods to solve the microscopic boundary value problems. We have reported on the software package and its parallel performance previously [19, 20]. In the current paper, for the first time, we provide weak scalability results for large production runs with parallel I/O on the complete machine. We also investigate the strong scalability of the FE2TI software, which has not been done before. For a detailed description of FETI-DP methods, see [8, 16–18].

5.1 Implementation Remarks

FE2TI is implemented using PETSc 3.5.2 [3], MPI, and hybrid MPI/OpenMP. Furthermore, we make use of the software libraries MUMPS [1, 2], UMFPACK [6], and PARDISO [26] as sequential (or parallel) direct solvers for subdomain problems. We also make use of inexact FETI-DP variants using BoomerAMG [14] from the hypre [7] package as a preconditioner of the FETI-DP coarse problem. On Blue Gene/Q, the software environment is compiled using the IBM XL C/C++ compilers using auto vectorization. When using UMFPACK as a direct solver for the subproblems, a large portion of the computing time is spent inside IBM's ESSL library, which implements efficient auto vectorization. In the computations presented here, we use piecewise linear brick elements (Q1) for all finite element discretizations. In our FE2TI implementation, an MPI_Comm_split is used to create subcommunicators for the computations on the RVEs (Representative Volume Elements). On Blue Gene/Q supercomputers, we use the environment variable

```
PAMID_COLLECTIVES_MEMORY_OPTIMIZED=1
```

to enable an efficient communicator split even for a large number of cores.

Each RVE is assigned to exactly one of the MPI subcommunicators, and the computations in 1. to 4. in Algorithm 1 can be carried out independently on each subcommunicator. This includes several parallel (inexact reduced) FETI-DP [17] setups and solves. Communication in between the several communicators is only necessary for the assembly of the linearized macroscopic problem (see 5. in Algorithm 1) and the update of the macroscopic variables (see 7. in Algorithm 1). The macroscopic solve (see 6. in Algorithm 1) is performed on each MPI rank redundantly, using a sparse direct solver. This is feasible due to the small macroscopic problem size. To assemble and solve the macroscopic problem on each MPI rank, the consistent tangent moduli and the averaged stresses in the macroscopic Gauß points have to be communicated to all ranks. Therefore, we have implemented a gather operation in two steps. First, the tangent moduli and stresses are averaged and collected on the master ranks of each RVE subcommunicator. This corresponds to an MPI_Reduce operation on each subcommunicator. In a second step, an MPI_Gather operation collects the data from the master ranks of the subcommunicators in the global master rank. This avoids a global all-to-all communication and only includes one MPI rank per RVE. Finally, we broadcast all tangent moduli and stresses from the global master rank to all MPI ranks. For some more details on the FE2TI implementation, see [19, 20].

A highly efficient parallel I/O strategy is also provided in the FE2TI package, based on HDF5 [32]. All data, as stresses and displacements on the RVEs, is written to one single parallel file, currently once every four macroscopic load steps. For a production run on the complete JUQUEEN, we have measured an I/O time of less than 2 % of the total runtime.

In all computations presented in this section, we consider two different Neo-Hooke materials. Note that for the results in this section, we do not use a CSDA approximation but rather the exact tangent. We have inclusions of stiff material ($E = 2100$, $\nu = 0.3$) in softer matrix material ($E = 210$, $\nu = 0.3$) and consider a realistic microstructure depicted in [20, Fig. 1]. The strain energy density function of the Neo-Hooke material W [15, 34] is given by

$$W(u) = \frac{\mu}{2}\left(\mathrm{tr}(\mathbf{F}^T\mathbf{F}) - 3\right) - \mu \ln(J) + \frac{\lambda}{2}\ln^2(J)$$

with the Lamé constants $\lambda = \frac{\nu E}{(1+\nu)(1-2\nu)}$, $\mu = \frac{E}{2(1+\nu)}$ and the deformation gradient $\mathbf{F}(x) := \nabla\boldsymbol{\varphi}(\mathbf{x})$; here, $\boldsymbol{\varphi}(\mathbf{x}) = \mathbf{x} + \mathbf{u}(\mathbf{x})$ denotes the deformation and $\mathbf{u}(\mathbf{x})$ the displacement of $\mathbf{x}$.

5.2 *Production Runs on the JUQUEEN Supercomputer*

First, we present three different production runs of different problem sizes in Table 2. Here, as a macroscopic problem, we discretize a thin plate with a rectangular hole with 8, 32, and finally 224 finite elements. This corresponds to a

full simulation of 64, 256, and finally 1792 RVEs in the corresponding macroscopic Gauß integration points. In 40–41 load steps, we apply a deformation of the plate of approximately 8 %. A visualization of the results of the largest production run has been previously reported on in [20, Fig. 1]. Considering only a few macroscopic load steps and disabling I/O, e.g., for checkpointing, we have already shown nearly optimal weak scalability for the FE2TI package [19, 20]. Here, for the first time, we present weak scalability for the production runs using full I/O (using HDF5 [32]), many load steps, an unstructured mesh on the macroscale, and a realistic microstructure from dual phase steel.

In our multiscale approach, the size of the RVE must be determined such that it is representative of the microstructure (sufficient size) and that it must capture all important features of the microstructure (sufficient resolution). Once the type of discretization is chosen, the number of degrees of freedom for the RVE is thus fixed. Here, each RVE has 823,875 degrees of freedom. In our computation, a problem on an RVE is then solved iteratively and in parallel, using 512 MPI ranks running on 256 cores, by a FETI-DP domain decomposition method using 512 subdomains. This choice results in an appropriate workload for each core. Therefore, the largest multiscale production run on the complete JUQUEEN at Forschungszentrum Jülich (917,504 MPI ranks on 458,752 cores) makes use of a total number of 1,476,384,000 degrees of freedom (of course representing a much larger full scale problem).

Neglecting the fact that we use slightly different dimensions for the macroscopic plate in the three different production runs, this set of production runs can also be viewed as a weak parallel scaling test. In addition to the total time to solution, we have also reported on the average runtime for the solution of a nonlinear RVE problem in Table 2. Here, we have a slight increase in the runtime of approximately 10 % when scaling from 1 to 28 racks. This is partially due to a small increase in I/O time and also slightly higher numbers of GMRES iterations in the FETI-DP solver, probably due to the larger and more complicated macroscopic problem. Nevertheless, for a complete production run including parallel I/O, these scalability results are satisfying. In Table 2, we also provide timings for the macroscopic solve. Since the macroscopic problem is currently solved redundantly on each core, this phase of the method does not scale. But even for the largest production run, the cost

Table 2 Complete FE^2 production runs using the FE2TI software; realistic microstructure in the RVEs; nonlinear elasticity model; 32 MPI ranks per node. *Avg. RVE Solve* denotes the average runtime to solve the nonlinear microscopic boundary value problems; *Avg. Macro Solve* denotes the average runtime of a direct solve on the macroscale

JUQUEEN—Complete FE^2 runs for elasticity						
#Racks	#MPI ranks	#RVEs	#Load steps	Time (s)	Avg. RVE solve (s)	Avg. macro solve (s)
1	32,768	64 RVEs	41*LS*	16,899	101.13	0.06
4	131,072	256 RVEs	41*LS*	17,733	105.95	0.22
28	917,504	1792 RVEs	40*LS*	18,587	112.48	1.54

for the macroscopic problem is currently negligible, i.e., it contributes less than 1% to the total runtime.

5.3 *Strong Scalability on JUQUEEN*

For the first time, we also present strong scalability results for the FE2TI software for a nonlinear model problem; see Table 3. Let us first describe the model problem used here. On the macroscale, we use the geometry and discretization of the second largest production run presented before in Table 2. Thus we have 256 microscopic boundary value problems (RVEs). In contrast to the previous production runs, we now consider smaller RVEs with 107 K degrees of freedom each. Each RVE has one stiff, spherical inclusion and is decomposed into 512 FETI-DP subdomains. The subdomains are thus quite small, only consisting of 375 degrees of freedom. Let us note that this setup avoids memory problems on the smallest partition (1024 MPI ranks). Let us remark that we always use 32 MPI ranks per BlueGene/Q node and thus less than 512 MByte are available per rank. This setup was found to be most efficient in [19, 20].

In our strong scaling test, we simulate one macroscopic load step which converges in three Newton steps. In 222 of the 256 RVE problems, 9 microscopic Newton steps are necessary for convergence during the complete macroscopic load step. For the remaining 34 Gauß points only 8 microscopic Newton steps are

Table 3 Strong scaling of FE^2 using the FE2TI software; nonlinear elasticity model; 32 MPI ranks per node. Macroscopic problem with 256 Gauß integration points; in each macroscopic integration point an RVE with 107K degrees of freedom is solved using 512 FETI-DP subdomains. Simulation of one macroscopic load step. *Time to Solution* denotes the total time needed for one FE^2 load step; *Eff.* denotes the parallel efficiency, where the total time to solution on 1 024 ranks is chosen as a baseline; *Speedup* denotes the speedup compared to the runtime on 1 024 cores; *Avg. FETI-DP Setup Time* denotes the average runtime necessary for a FETI-DP setup for one linearized system on an RVE; *Avg. Ass. Time* denotes the average runtime of the assembly of one linearized system on an RVE; *Avg. Solve Time* denotes the average iteration time to solve one linearized system on an RVE; all averages consider all linearized systems occurring in all microscopic Newton steps

Strong scaling on JUQUEEN						
MPI ranks	Time to solution (s)	Eff. (%)	Speedup	Avg. FETI-DP setup time (s)	Avg. ass. time (s)	Avg. solve time (s)
1024	1568.9	100	1.00	14.98	44.29	21.08
2048	822.0	95	1.91	6.97	22.13	11.54
4968	431.7	91	3.63	3.51	11.07	5.65
8192	225.0	87	6.97	1.85	5.54	3.05
16,384	138.7	71	11.39	1.04	2.77	2.32
32,768	90.0	54	17.42	0.61	1.38	1.43
65,536	40.4	61	38.81	0.39	0.69	0.67
131,072	35.6	34	44.10	0.29	0.35	0.65

performed. This means, depending on the RVE, we perform 11 or 12 FETI-DP setups including problem assembly, while 35 or 36 FETI-DP solves are necessary. Let us recall that we have to perform one FETI-DP setup and solve per microscopic Newton step. Additionally, after convergence on the microscale, we have to compute the consistent tangent moduli (see 4. in Algorithm 1). Therefore, for each of the three macroscopic Newton steps, one further FETI-DP setup and nine FETI-DP solves with different right hand sides are necessary. This sums up to the mentioned number of FETI-DP setups and solves on each microstructure. In average, we have 44.8 GMRES iterations for each FETI-DP solve. Let us remark that we consider all macroscopic as well as microscopic Newton iterations as converged, if the l_2-norm of the Newton update is smaller than $1e-6$.

Since the lion's share of the runtime of the FE2TI package is spent in the assembly of the microscopic problems and in FETI-DP, the strong scalability is dominated by three phases: the problem assembly on the RVEs, the FETI-DP setup, and the FETI-DP solve; see also [21] for a detailed discussion on the strong scaling behavior of (ir)FETI-DP methods. Therefore, we provide detailed timings for those three phases in Table 3. We obtain, as it can be expected, perfect scalability for the assembly phase and also convincing results for the FETI-DP setup phase. The FETI-DP solution phase scales well up to 65 K ranks. Scaling further up to 131 K ranks the additional benefit is small. These results are also depicted in Fig. 7. All in all, this leads to a satisfying strong scaling behavior of the complete FE2TI package from 1 K up to 65 K ranks with 61 % parallel efficiency and a speedup of 38.8; see also Fig. 8. Let us finally remark that the FE2TI package can thus solve 256 times 36 linear systems with 107 K degrees of freedom in approximately 40 s on 65 K MPI ranks and 32 K BlueGene/Q cores.

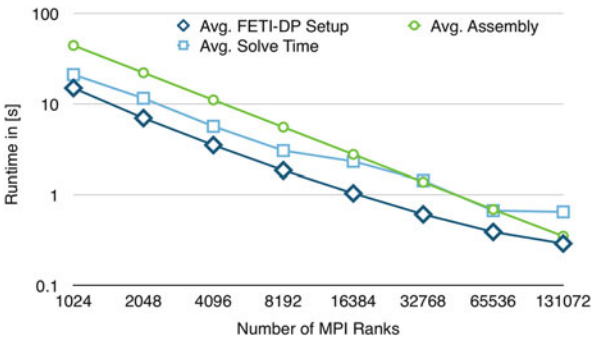

Fig. 7 Strong scalability of the FE2TI software. Figure corresponds to data from Table 3. Scalability of the different phases of the RVE solver FETI-DP

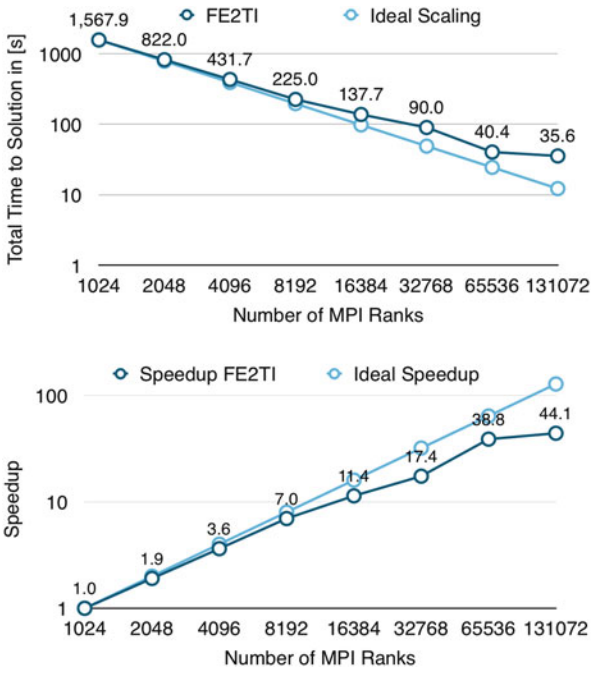

Fig. 8 Strong scalability of the FE2TI software. Figure corresponds to data from Table 3. *Top*: Total time to solution. *Bottom*: Speedup

6 Conclusion

We have presented two steps towards the realistic two-scale simulation of dual-phase steel. First, we have discussed our isotropic, thermodynamically-consistent, thermo-elastoplastic material model, based on [28], to be employed in the multiscale simulation of dual-phase steel sheets. A numerical differentiation scheme, which relies on the complex step derivative approximation approach, was used to compute the tangent stiffness matrices in the thermo-mechanical simulations. It allows to obtain locally quadratic convergence of Newton's method. Within this setting, a one-way coupling scheme is utilized to increase the efficiency in the multiscale analysis of the steel sheet subjected to inhomogeneous deformations. The multiscale analysis presented here indicates that the higher level of information involved in the micro-level computation leads to a more accurate assessment of critical states during the forming process. The resulting mechanical field distributions help to identify areas in the microstructure geometry where concentrations of stress or strains may lead to initialization of failure. This information is not accessible by purely phenomenological material models and limits their predictive capabilities. Additionally, the comparison between various approaches at the micro-level show that, for DP steels, where the thermal properties of the phases are almost identical, for the considered nominal strain rates ($\dot{\bar{\varepsilon}} \approx 10^{-2}\,\mathrm{s}^{-1}$), the thermo-mechanical consideration does not yield significantly different response than the purely mechanical one. Thus, for cases

similar to the one presented here, considering only mechanics at the microscale can reduce computational effort substantially without significant loss of accuracy.

Second, we have presented the FE2TI software package for the two-scale simulation of steel. The package allows one-way coupling, as described above, as well as two-way, two-scale coupling using the FE^2 approach. We have discussed weak scalability for up to 458,752 cores for the fully coupled FE^2 production runs using full I/O, many load steps, an unstructured mesh on the macroscale, and a realistic microstructure from dual phase steel. As a result of the previous considerations, in these computations, we could neglect temperature effects. We have also presented strong scalability results for the FE2TI software using up to 131 072 cores of the JUQUEEN supercomputer.

Acknowledgements This work was supported by the German Research Foundation (DFG) through the Priority Program 1648 "Software for Exascale Computing" (**SPPEXA**), projects BA 2823/8-1, KL 2094/4-1, RH 122/2-1, and SCHR 570/19-1.

The authors gratefully acknowledge the Gauss Centre for Supercomputing (GCS) for providing computing time through the John von Neumann Institute for Computing (NIC) on the GCS share of the supercomputer **JUQUEEN** [30] at Jülich Supercomputing Centre (JSC). GCS is the alliance of the three national supercomputing centres HLRS (Universität Stuttgart), JSC (Forschungszentrum Jülich), and LRZ (Bayerische Akademie der Wissenschaften), funded by the German Federal Ministry of Education and Research (BMBF) and the German State Ministries for Research of Baden-Württemberg (MWK), Bayern (StMWFK) and Nordrhein-Westfalen (MIWF).

The use of **CHEOPS** at Universität zu Köln and of the **High Performance Cluster** at Technische Universität Bergakademie Freiberg are also gratefully acknowledged. Furthermore, the authors D. Balzani and A. Gandhi appreciate S. Prüger for helpful scientific discussions.

References

1. Amestoy, P.R., Duff, I.S., Koster, J., L'Excellent, J.Y.: A fully asynchronous multifrontal solver using distributed dynamic scheduling. SIAM J. Matrix Anal. Appl. **23**(1), 15–41 (2001)
2. Amestoy, P.R., Guermouche, A., L'Excellent, J.Y., Pralet, S.: Hybrid scheduling for the parallel solution of linear systems. Parallel Comput. **32**(2), 136–156 (2006)
3. Balay, S., Brown, J., Buschelman, K., Gropp, W.D., Kaushik, D., Knepley, M.G., McInnes, L.C., Smith, B.F., Zhang, H.: PETSc Web page. http://www.mcs.anl.gov/petsc (2014)
4. Balzani, D., Gandhi, A., Tanaka, M., Schröder, J.: Numerical calculation of thermo-mechanical problems at large strains based on complex step derivative approximation of tangent stiffness matrices. Comput. Mech. **55**, 861–871 (2015)
5. Balzani, D., Scheunemann, L., Brands, D., Schröder, J.: Construction of two- and three-dimensional statistically similar RVEs for coupled micro-macro simulations. Comput. Mech. **54**, 1269–1284 (2014)
6. Davis, T.A.: Direct Methods for Sparse Linear Systems. SIAM, Philadelphia (2006)
7. Falgout, R.D., Jones, J.E., Yang, U.M.: The design and implementation of hypre, a library of parallel high performance preconditioners. In: Bruaset, A.M., Bjorstad, P., Tveito, A. (eds.) Numerical Solution of Partial Differential Equations on Parallel Computers. Lecture Notes in Computational Science and Engineering, vol. 51, pp. 267–294. Springer, Berlin (2006). http://dx.doi.org/10.1007/3-540-31619-1_8

8. Farhat, C., Lesoinne, M., LeTallec, P., Pierson, K., Rixen, D.: FETI-DP: a dual-primal unified FETI method – part I: a faster alternative to the two-level FETI method. Int. J. Numer. Methods Eng. **50**, 1523–1544 (2001)
9. Feyel, F., Chaboche, J.: Fe^2 multiscale approach for modelling the elastoviscoplastic behaviour of long fibre SiC/Ti composite materials. Comput. Methods Appl. Mech. Eng. **183**, 309–330 (2000)
10. Fish, J., Shek, K.: Finite deformation plasticity for composite structures: computational models and adaptive strategies. Comput. Methods Appl. Mech. Eng. **172**, 145–174 (1999)
11. Geers, M., Kouznetsova, V., Brekelmans, W.: Multi-scale first-order and second-order computational homogenization of microstructures towards continua. Int. J. Multiscale Comput. **1**, 371–386 (2003)
12. Golanski, D., Terada, K., Kikuchi, N.: Macro and micro scale modeling of thermal residual stresses in metal matrix composite surface layers by the homogenization method. Comput. Mech. **19**, 188–201 (1997)
13. Griewank, A., Walther, A.: Evaluating Derivatives. Society for Industrial and Applied Mathematics, 2nd edn. (2008). http://epubs.siam.org/doi/abs/10.1137/1.9780898717761
14. Henson, V.E., Yang, U.M.: BoomerAMG: a parallel algebraic multigrid solver and preconditioner. Appl. Numer. Math. **41**, 155–177 (2002)
15. Holzapfel, G.A.: Nonlinear Solid Mechanics. A Continuum Approach for Engineering. John Wiley and Sons, Chichester (2000). http://opac.inria.fr/record=b1132727
16. Klawonn, A., Rheinbach, O.: Robust FETI-DP methods for heterogeneous three dimensional elasticity problems. Comput. Methods Appl. Mech. Eng. **196**(8), 1400–1414 (2007)
17. Klawonn, A., Rheinbach, O.: Highly scalable parallel domain decomposition methods with an application to biomechanics. ZAMM Z. Angew. Math. Mech. **90**(1), 5–32 (2010). http://dx.doi.org/10.1002/zamm.200900329
18. Klawonn, A., Widlund, O.B.: Dual-primal FETI methods for linear elasticity. Commun. Pure Appl. Math. **59**(11), 1523–1572 (2006)
19. Klawonn, A., Lanser, M., Rheinbach, O.: EXASTEEL – computational scale bridging using a FE^{2}TI approach with ex_nl/FE^2. Technical report FZJ-JSC-IB-2015-01, Jülich Supercomputing Center, Germany (2015). https://juser.fz-juelich.de/record/188191/files/FZJ-2015-01645.pdf. In: Frings, Brian J.N. Wylie (eds.) JUQUEEN Extreme Scaling Workshop 2015. Dirk Brömmel and Wolfgang
20. Klawonn, A., Lanser, M., Rheinbach, O.: FE2TI: Computational Scale Bridging for Dual-Phase Steels (2015). Accepted for publication to the proceedings of the 16th ParCo Conference, Edinburgh. To be published in Advances in Parallel Computing
21. Klawonn, A., Lanser, M., Rheinbach, O.: Towards extremely scalable nonlinear domain decomposition methods for elliptic partial differential equations. SIAM J. Sci. Comput. **37**(6), C667–C696 (2015)
22. Miehe, C.: Numerical computation of algorithmic (consistent) tangent moduli in large-strain computational inelasticity. Comput. Methods Appl. Mech. Eng. **134**, 223–240 (1996)
23. Miehe, C., Schröder, J., Schotte, J.: Computational homogenization analysis in finite plasticity. simulation of texture development in polycrystalline materials. Comput. Methods Appl. Mech. Eng. **171**, 387–418 (1999)
24. Moulinec, H., Suquet, P.: A numerical method for computing the overall response of nonlinear composites with complex microstructure. Comput. Methods Appl. Mech. Eng. **157**, 69–94 (1998)
25. Pérez-Foguet, A., Rodríguez-Ferran, A., Huerta, A.: Numerical differentiation for local and global tangent operators in computational plasticity. Comput. Methods Appl. Mech. Eng. **189**, 277–296 (2000)
26. Schenk, O., Gärtner, K.: Two-level dynamic scheduling in PARDISO: improved scalability on shared memory multiprocessing systems. Parallel Comput. **28**(2), 187–197 (2002)
27. Schröder, J.: A numerical two-scale homogenization scheme: the FE^2-method. In: J. Schröder, K. Hackl (eds.) Plasticity and Beyond – Microstructures, Crystal-Plasticity and Phase Transitions. CISM Lecture Notes 550. Springer, Wien (2013)

28. Simo, J., Miehe, C.: Associative coupled thermoplasticity at finite strains: formulations, numerical analysis and implementation. Comput. Methods Appl. Mech. Eng. **98**, 41–104 (1992)
29. Smit, R., Brekelmans, W., Meijer, H.: Prediction of the mechanical behavior of nonlinear heterogeneous systems by multi-level finite element modeling. Comput. Methods Appl. Mech. Eng. **155**, 181–192 (1998)
30. Stephan, M., Docter, J.: JUQUEEN: IBM Blue Gene/Q® Supercomputer System at the Jülich Supercomputing Centre. JLSRF 1, A1. http://dx.doi.org/10.17815/jlsrf-1-18 (2015)
31. Tanaka, M., Fujikawa, M., Balzani, D., Schröder, J.: Robust numerical calculation of tangent moduli at finite strains based on complex-step derivative approximation and its application to localization analysis. Comput. Methods Appl. Mech. Eng. **269**, 454–470 (2014)
32. The HDF Group: Hierarchical Data Format, version 5. http://www.hdfgroup.org/HDF5/ (1997-NNNN)
33. Wriggers, P., Miehe, C., Kleiber, M., Simo, J.: On the coupled thermomechanical treatment of necking problems via finite element methods. Int. J. Numer. Methods Eng. **33**, 869–883 (1992)
34. Zienkiewicz, O.C., Taylor, R.L.: The Finite Element Method for Solid and Structural Mechanics. Elsevier, Oxford (2005)